Wall shear stress measurements using a MTV-based plenoptic microscope

P. D. Huck*, C. Fort, P. M. Bardet

Department of Mechanical and Aerospace Engineering, The George Washington Unviersity, USA
*Corresponding author: peterdhuck@gwu.edu

Keywords: Computational Imaging, Plenoptic Imaging, Micro MTV, Wall Shear Stress

ABSTRACT

In this contribution, we describe the first ever microscopic Molecular Tagging Velocimetry (MTV) measurements using Integral Imaging. This technique permits the measurement of the 3D-2C velocity field in an axi-symmetric stagnation jet and observed profiles agree well with analytical predictions. Standard reconstruction algorithms are compared against more advanced deconvolution algorithms and substantial improvements in reconstructed probe resolution are obtained. Integral imaging is compared with a scanning confocal microscope which serves as a basis of comparison and good agreement is achieved. The flow facility was designed for a low Reynolds number, but with an adjustable viscous length scale comparable with higher Reynolds number flows. Our instrument proves capable of resolving viscous length scales on the order of 30 micrometers which can be improved by increasing the numerical aperture of the microscope objective.

1. Introduction

Parasitic frictional drag due to fouling can increase overall flow resistance, increasing shaft power requirements in naval platforms by up to 85% (Schultz, 2007). Numerical modeling informed by high resolution data of these processes is therefore extraordinarily important. However, measurements in highly turbulent boundary layers are notoriously difficult as the length scales at the Reynolds numbers of interest are on the order of a few micrometers. To address these issues, several techniques have been used to obtain wall shear stress (WSS) measurements. For example, WSS may be inferred by heat-transfer measurements (H. Kreplin, 1994) pressure drops (Huang et al., 2012), or mean velocity profiles using Clauser charts. However, those methods are indirect or assume a canonical boundary layer profile, which may not be applicable to complex geometries.

In this paper we propose direct measurements of WSS using Molecular Tagging Velocimetry (MTV) focused on the viscous sub-layer. The deformation of tagged lines of chemical tracers at the wall permits direct measurement of the velocity gradient. There, MTV has higher spatial resolution than particle-based approaches such as laser Doppler velocimetry (LDV) or particle image velocimetry (PIV). The technique presented here is volumetric and resolves the WSS distributed over a surface area. The novelty of the optical measurements presented here will be benchmarked against standard microscopy and the analytical (Schlichting) solution for an axi-symmetric stagnation point flow (Schlichting, 2017).

2. Experimental Facility

To generate steady boundary layers with a controllable thickness, an axi-symmetric stagnation jet facility has been designed following standard-practice design rules for low speed flow facilities described in section 2.1. The facility was designed based on resolution capabilities of the optical system and informed by Schlichting's axi-symmetric boundary layer theory (Schlichting, 2017) presented in section 2.2.

2.1. Facility Design

Water at ambient (20°C) temperature enters a settling chamber through a diffuser. The settling chamber consists of a honeycomb and successive mesh screens. It is followed by a contracting nozzle. The diffuser has an area ratio of 9 and a cone angle of $2\theta = 10^{\circ}$ which corresponds to minimal friction losses for a gradual conical expansion region (Gibson, 1910). The adverse pressure gradient in the diffuser is sufficiently small that screens are not required to prevent flow separation (Mehta & Bradshaw, 1979). A 25.4 mm long honeycomb with a 3.2 mm diameter immediately follows the diffuser to straighten the flow and the length-to-diameter ratio of nearly eight satisfies optimal design criteria (Mehta & Bradshaw, 1979). The first of two stainless steel screens is placed four honeycomb diameters downstream of honeycomb to prevent the development of a wake. The mesh has a near optimal solidity of 56% (Mehta & Bradshaw, 1979), with a mesh spacing 0.635 mm and wire diameter 0.165 mm. The two screens are spaced by 40 mesh sizes to allow the RMS turbulent fluctuations to decay to 2.5% of the free stream value and minimize the development of boundary layers on the side walls (Barlow et al., 1999; Pope, 2010). The second screen is placed at a distance of 0.3 pipe diameter from the contraction section, in agreement with Mehta & Bradshaw (1979). The nozzle contraction is a 5th order polynomial and has a 9:1 contraction ratio over a 1.75 nozzle diameters length. The nozzle is 16.8 mm in diameter designed for a 1 m/s bulk velocity and is placed 10 mm from the UV-grade quartz window, creating an axi-symmetric stagnation point flow (sketched in Figure 1). A 1/2 HP (0.373 kW) centrifugal pump powered by a Variable Speed Drive permits bulk velocities between $W_0 = [0.3 - 1.0]\ \mathrm{m/s}$ at the nozzle. The optical axis of the device used in this contribution is oriented parallel with the z-axis of the stagnation point flow.

2.2. Axi-symmetric Stagnation Jet : Theory

When considered partitioned into two regions, an inviscid outer layer and a viscid inner layer, the axi-symmetric boundary layer has an analytic self-similar solution derived by Schlichting (2017)

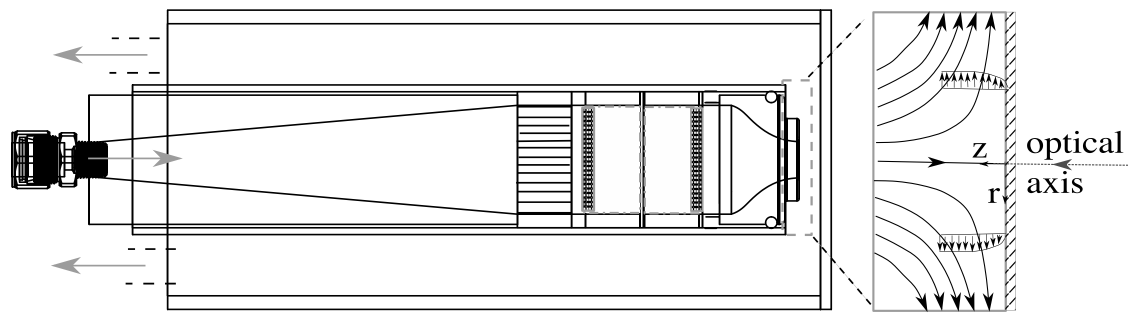

Figure 1. Stagnation jet facility. A 10 degree diffuser begins the flow conditioning, followed by a honeycomb and two mesh grids. A 9:1 converging nozzle creates an axi-symmetric stagnation point flow at the quartz optical window. The optical axis of the imager is made orthogonal to the wall.

which we summarize here. The velocity distribution of an axi-symmetric, inviscid, stagnation flow is

$$U = \alpha r, \quad V = 0, \quad W = -2\alpha z \tag{1}$$

where $\alpha = W_0/L$ characterizes the stagnation jet and is composed of the bulk velocity W_0 and distance from the nozzle to the wall L. While this equation satisfies continuity and the Navier-Stokes equation, it does not satisfy the no-slip boundary condition which requires that viscosity is accounted for. Schlichting (2017) proposed the ansatz,

$$u = Uf'(\eta), \quad w = -2\sqrt{\alpha\nu} \tag{2}$$

where $\eta = \sqrt{\alpha/\nu}z$. The third order, ordinary differential equation that satisfies continuity and the Navier-Stokes equation as well as boundary conditions including no-slip, zero-flux at the wall, and overlap of the inviscid and viscid solutions as $\eta \longrightarrow \infty$ is given by,

$$f^{'''} + 2ff^{''} + 1 - f^{'2} = 0. \tag{3}$$

We note that the non-dimensional radial velocity $u/U = f^{'}(\eta)$ in Eq. (2) is independent of r and is therefore self-similar.

Numerically integrating Eq. (3) gives the boundary layer thickness (ℓ) and viscous length scale (ℓ_ν) of the axi-symmetric :

$$\ell = 2.8\ (\nu/\alpha)^{1/2}, \quad \ell_\nu = 0.93\ (\alpha U^2/\nu^3)^{-1/4} \tag{4}$$

where the latter equation can be derived from the fact that $f^{''} = 1.312$ at $\eta = 0$. From these equations, we are able to predict the length scales of interest for the stagnation-jet facility. These are given in Table 1 for the present experimental parameters. In addition, turbulent length scales of boundary layers in a turbulent pipe flow with (van Doorne & Westerweel, 2007) and a turbulent plate (Winkel et al., 2012) are given for comparison. While the present flow is clearly not turbulent, the viscous scales are on the order of fully developed turbulent flows. We note that by decreasing the value wall-to-nozzle distance we can bring ℓ_ν to within a factor of 2.7 of the data of Winkel et al. (2012). The goal of this facility is not to reproduce the turbulence of these high Re_τ flows, but rather to validate that the diagnostics employed can accurately resolve velocity gradients with viscous length scales of the order of magnitude of a high-Reynolds number turbulent flow.

Table 1. Boundary layer thickness (ℓ), viscous length scale (ℓ_ν), and Karman numbers $Re_\tau = \ell/\ell_\nu$ for the present stagnation jet facility as well as turbulent pipe flow van Doorne & Westerweel (2007) and turbulent plate flow Winkel et al. (2012). All measurements are conducted in water.

Facility & Author	ℓ [mm]	ℓ_ν [mm]	$Re_\nu = \ell/\ell_\nu$ [$-$]
Stagnation Jet, Present	0.60-0.42	0.029-.017	20-24
Pipe, van Doorne & Westerweel (2007)	20	0.11	180
Plate, Winkel et al. (2012)	70-105	0.0047-.00172	15-61$\times 10^3$

3. Experimental Methods

The laser-induced fluorescence of rhodamine 6G (R6G) molecular tracers are used to probe the velocity field in the stagnation jet. This spectroscopic technique is known as MTV and is discussed in Section 3.1. The principle of integral microscopy is then employed to access 3D-2C, distributed measurements of the velocity gradients at the wall. The design criteria for instrument the stagnation jet facility is presented in Section 3.2 and the fundamentals of the 3D reconstruction technique is discussed in Section 3.3.

3.1. Photobleaching Molecular Tagging Velocimetry

MTV relies on the synchronization of two lasers, a "write" and a "read" pulses, to measure velocity. Here, the 10 ns write pulse is from a frequency-tripled Nd:YAG laser (355 nm) that irreversibly destroys (photobleaches) R6G molecules uniformly dissolved in water (Fort & Bardet, 2021) at a concentration of 400 µg/L (835 nM). A frequency-doubled Nd:YLF laser (527 nm) provides the read pulses, illuminating the remaining R6G in the region of interest. R6G fluoresces at 550 nm and is easily imaged by common scientific cameras. The result is a tagged region that appears dark due to photobleaching against the bright fluorescent background. For a small time interval between the read and write pulses, the tagged region initially provides a regularly spaced, straight pattern that can be compared with a subsequent, deformed pattern captured by a second read pulse. Displacement of the deformed tagged line is captured with this write-read-read sequence and measuring the time of flight gives direct access to the local flow velocity. The details of the photobleaching process (write) of R6G and optimization have been extensively reported by Fort & Bardet (2021). The laser delivery scheme can be seen in Figure 1. The UV beam arrives by a series of mirrors (Figure 2a) and is driven up towards the microscope where it is turned into the optical axis of the microscope objective which is orthogonal to the circular optical window. We denote this configuration *co-axial* due to the alignment of the microscope optical axis and the sensing probe, the write (UV) beams. The green laser arrives at an oblique angle to the optical axis of the microscope either through a 5X Mitutoyo long working distance NA = 0.14 objective (pictured, Figure 2b) or in a 3 mm diameter beam at a 45 degree angle to the wall. In what follows we have implemented

(a) (b)

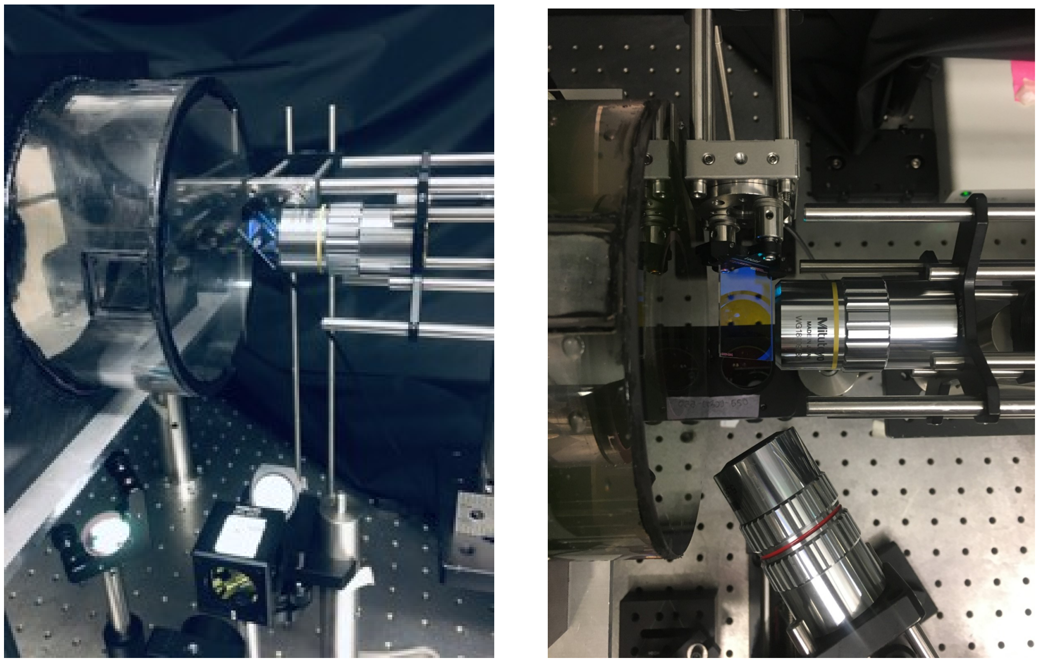

Figure 2. Stagnation jet facility with optical components. (a) Side view of facility. UV beam arrives by several mirrors before being driven up into a dichroic mirror (recently replaced by dichroic cube) to align with the optical axis of the microscope objective. (b) Top view of facility objective lens (yellow ring) is co-axial with UV beam. Green light delivered obliquely through 5X NA=0.13 Mitutoyo long working distance objective or by a single 3 mm beam at 45 degrees to the wall.

the latter "read" format without the microscope objective.

Global information of the flow topology is lost when relying on a single beam. Slotted beam blockers have been used to illuminate multiple lines with a single laser beam. However, the smallest repeatable diameter of these beamlets is on the order of 100 µm and only a fraction of the available laser energy is used. Talbot-effect structured illumination (TESI) Fort et al. (2020) bypasses the need for a beam-blocking device. Instead, TESI relies on the interference phenomenon of a laser beam incident on a microlens array (MLA) to create a pattern of parallel beamlets. The beamlet size, is diffraction limited instead of limited by the size of the mechanical aperture of a beam-blocker. At the focal length of the MLA $f_m = 18.8$ mm with a spacing between lenses of $p_0 = 300$ µm, the waist of the beamlets is diffraction limited and given by: $w_0 = A_m 2\lambda/\pi \mathrm{NA}_{ml}$ where A_m accounts for aberrations in the optical assemblies and $\mathrm{NA}_{ml} = w_i/2f_m$ is the numerical aperture of each micro lens. The incident light on the individual lens in the array is roughly equal to the pitch of the array, i.e. $w_i \simeq p_0$. For an aberration-free system ($A_m \sim 1$) under UV light (355 nm), the expected beam width at the focal plane is $w_0 \sim 28$ µm, which represents the small-scale resolution of the pattern. However TESI allows to reach higher resolution and has been demonstrated by Fort (2021) and currently represents the highest resolution of any MTV deployment.

TESI preserves the periodic structure of an MLA with lens spacing p_0 at the Talbot planes separated by the Talbot distance:

$$z_T = p_0^2/\lambda. \tag{5}$$

While it is possible to make measurements at the focal plane of the MLA, a diffraction Airy pattern with secondary intensity lobes is present. The multiple lobes can decrease the signal-to-noise ratio and be detrimental for identifying the tagged lines. At a distance $z = f_m + z_T$, the focused beamlets of the MLA are reproduced without the Airy pattern. Additionally, the beamlets stay focused for a longer distance than the typical Rayleigh range for focused beams. For a laser beam of initial diameter w_L, the number of beamlets n at the Talbot distance is equal to the number of microlenses contributing to the pattern $n_0 \approx w_L/p_0$ if the divergence of the individual lenses is not too large. In essence TESI allows a "refocusing" of the individual beamlets at a distance $z_T = 254$ mm from the MLA, which permits a convenient experimental implementation with long projection distances and without the presence of an Airy pattern (Figure 3). In addition to self-images, patterns with a varying periodicity $p(z)$ are observed at fractional Talbot distances $z = (Q/R + K)z_T$ according to Eq. 2, with Q and R positive coprime integers, and $K \geq 0$ a third integer.

$$p[z = f_m + (Q/R + K)z_T] = p_0/R. \tag{6}$$

Equations (5) and (6) highlight the flexibility of the lines generation scheme. With TESI, one can acquire the preferred spatial period (we have achieved periodicity as small as 15 µm) by controlling the distance between the focal plane of the MLA and the measurement section or/and by changing the MLA. In this paper, a 2D beamlet grid with 300-µm square pitch is demonstrated, for the first time, using 300-µm-pitch spherical-microlens array.

In summary, TESI addresses two important issues in MTV. First, it provides an unprecedented probe resolution, the beamlet size, for velocimetry measurements. From Table 1, a beamlet width of 28 µm is on the order of the viscous length scale for the stagnation jet facility. If one assumes the resolution criteria that the sensing length be less than about $10\ \ell_\nu$ (Talamelli et al., 2009), this probe length permits resolution of the viscous lengths in the highest Re_τ facilities. By increasing the numerical aperture of the micro lenses ($\mathrm{NA_{ml}}$, we can achieve these length scales with no assumptions on the validity of the sensing length. Second, TESI provides a controllable discretization length for the velocity field that is determined by the recovered periodicity of the MLA. For the current implementation, at the Talbot plane z_T in Eq. 6, the periodicity is that of the micro lens array $p = p_0 = 300$ µm. However, at a fractional plane (*e.g.* $K = 0,\ Q = 1,\ R = 4$) the beam spacing is now $p = p_0/4 = 75$ µm, which is on the order of the vector spacing (33 µm) achievable in Tomographic PIV with microscope objectives (Kim et al., 2011, 2013). The irradiance of the green beam is 0.0014 $\mathrm{J/cm^2}$ and the irradiance of a single UV beamlet is 0.85 $\mathrm{J/cm^2}$.

While the write stage of MTV permits resolution on par with other state-of-the-art techniques, it is important to ensure that this resolution is matched by the imaging technique employed. In Sec. 3.2 we address the design criteria for an integral microscope and Sec. 3.3 will present the 3D reconstruction techniques employed to achieve this resolution.

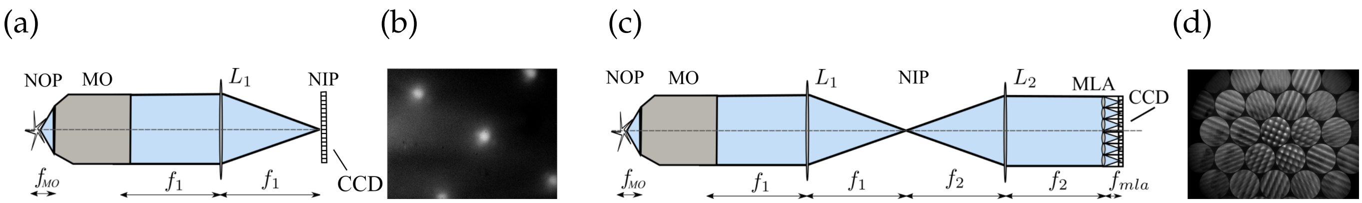

Figure 3. Different optical implementations for photobleaching microscopy. The UV (write) and Green (read) beams are oriented in the optical axis of each microscope. (a) Confocal microscope and (b) background subtracted (and inverted) raw image. (c) FIMic implementation and (d) background subtracted (and inverted) raw image.

3.2. Integral Microscopy

Distributed MTV measurements are achieved using Fourier integral microscopy (FIMic). The FIMic approach is a class of light field, or plenoptic imaging; it allows volumetric measurements with the use of a single camera (Llavador, et al., 2018). It has the advantage over the so-called plenoptic 1.0 approach (Ng, et al., 2005) in that it forms perspective views directly instead of an intermediate computational step, simplifying the post-processing. From these perspective views, tomographic reconstruction algorithms can be used to create a 3D rendering of the scene. FIMic trades a slight decrease in resolution, compared to traditional confocal microscopes, for a field that can be computationally reconstructed in 3D.

A high NA, infinity-corrected microscope objective captures the scene and an MLA is projected to the aperture (or Fourier) plane of the objective by a $4-f$ relay system. Each microlens creates a different perspective view of the same image formed by the main lens as sketched in Figure 3(c). The perspective views are called "elemental images". Here the objective optical axis is collinear with the UV laser beamlets responsible for photobleaching the R6G. Figure 3(d) shows the elemental images where perspective of the beamlets are visible. We note that the native object plane (NOP) is conjugate with the native image plane (NIP) where we can equivalently place a scientific camera (instead of the second lens and MLA) in which case the set-up reduces to a standard, confocal microscope (Fig. 3a-b). Below, the lateral, depth of focus, and axial resolution are described for a FIMic and compared with the confocal microscope base case.

In a classic microscope (CM), the depth of field (DoF, Δ_{z0}) has a wave optics contribution Δ_{wave}, as well as a geometrical optics term Δ_{geo} (Levoy et al., 2006):

$$\Delta_{z0} = \Delta_{wave} + \Delta_{geo} = \lambda n/(\mathrm{NA}^2) + n/M\mathrm{NA}p_{pix} \quad (7)$$

where λ is the light wavelength, n the index of refraction, and p_{pix} is the pixel pitch. If the pixels are small enough to not be a limiting factor, the DoF of the microscope is diffraction limited and reduces to $\Delta_{z0} \simeq \Delta_{wave}$. For the infinity-corrected Mitutoyo 10X NA = 0.28 objective used here, this corresponds to $\Delta_{z0} = 5.9$ µm and is on the order of a typical ℓ_ν at large Reynolds number. Similarly, the lateral resolution will be diffraction limited:

$$R_{xy0} = 0.47\lambda/\mathrm{NA} = 0.9\ \mu\mathrm{m} \quad (8)$$

Table 2. Camera parameters for confocal microscopy (CM) and Fourier Integral Microscope (FIMic). A higher NA objective can be used in FIMIC to increase resolution of the imager.

	Lateral Resolution (R_{xy}) [μm]	Depth of Field (Δ_z) [μm]	Axial resolution (R_z) [μm]
CM	0.9	9.0	9.0
FIMic	5.0	283.0	34.0

Since the CM is focused in a single plane, the DoF and the axial resolution (R_{z0}) are equal by definition. These values are given in Table 1 and compared with the FIMic implementation.

In the FIMic optical implementation, the MLA effectively subsamples the aperture stop (D_{as}) of the microscope objective in N sub-apertures given by $N = D_{as}/p$ where p is the pitch of the MLA. Here, $N = 5.6$ and corresponds to the middle row of orthographic views in Figure 3(d).

These N sub-apertures are each orthographic, meaning that they individually offer no perspective effects, but collectively increase the angular information of the microscope at the price of slightly reduced spatial resolution. The effective NA of the host microscope is reduced: $\mathrm{NA}_{eff} = \mathrm{NA}/N$. The effective lateral resolution is slightly degraded with respect to the CM, but is still adequate to resolve motion on the order of the viscous scale in the near wall region.

$$R_{xyF} = NR_{xy0} = 5.0\ \mu\mathrm{m} \tag{9}$$

The DoF of the FIMic is increased by a factor of N^2 with respect to the CM,

$$\Delta_{zF} = \Delta_{z0}N^2 = 283\ \mu\mathrm{m} \tag{10}$$

The ability of the FIMic to perform an optical sectioning of flow in the direction of the optical axis permits 3D measurements and is characterized by the axial resolution (R_{zF}) of the imager. Practically, this means that a there is an axial distance R_{zF} over which emission of a single point source contained within the slice falls by a factor of, say, $1/2$. Treating the MLA as a pin-hole array this distance has been derived using geometric optics (Scrofani et al., 2018),

$$R_{zF} = \gamma \frac{p_{pix}}{p} \Big(\frac{f_{mo}^2}{f_{mla}}\Big) \Big(\frac{f_2}{f_1}\Big)^2, \tag{11}$$

where γ is a constant on the order of unity related to the reconstruction procedure (see sec. 3.3). The resolution of the instrument is recapitulated in table 2.

3.3. 3D Reconstruction

In this section we compare two methods for reconstruction the 3D irradiance field. First we describe the Shift and Multiply (SM) approach which is a computationally inexpensive way to reconstruct the 3D lightfield. We also discuss the deconvolution-based approach, which are computationally more demanding, but handles out-of-plane fluorescence more efficiently.

Shift and Multiply (SM) Algorithm

The elemental (or perspective) views are used for tomographic reconstruction of the scene. Adopting a Cartesian coordinate system for simplicity, tomographic reconstruction is the attribution of voxel in (x,y,z) to a set of pixels on each elemental image. Several techniques are available to obtain the pixel-to-voxel correspondence. The simplest of which is the additive line of sight (ALOS) algorithm, which has also been termed the shift and sum (SS) in the light field literature (Hong et al., 2003). Similar to the tomographic reconstruction literature where multiplicative line of sight (MLOS) is used Worth & Nickels (2008); Atkinson & Soria (2009), the SM algorithm performs better at removing out of plane light. We discuss the principle of the SM algorithm below.

The proposed method considers each elemental image as a projection of the 3D scene through a virtual pinhole located a distance f_e from the sensor plane. The goal is then to achieve an inverse mapping of the pixels on each elemental image into object space. Pixels are extracted from the elemental images and displayed as the corresponding voxels in (x,y,z). As the pixels are projected through the pinhole using geometric optics, the regions of eventual overlap between elemental images are multiplied. This forward projection manifests as a shift of pixels from a neighboring elemental image onto the reference elemental image. Hence, a greater pixel shift onto the reference image accounts for regions of space with a greater distance from the pixel plane. In practice the central elemental image is the reference image (Figure 3d) and the twelve surrounding elemental images are shifted onto the reference to form the reconstructed plane. The lateral extent of the voxel is given by the lateral resolution of FIMic (R_{xyF}), which remains constant over the entire depth of field due to the nature of the orthographic view. The extent of the voxel in the direction of the optical axis z can be shown to be equal to Equation 11 where γ is the minimum pixel shift between the images, and is naturally equal to unity.

One may interpret the SM reconstruction in terms of the disparity, or pixel shift d_p, between the projection object at the NOP to the NIP on two elemental images. Axial distance from the NIP to NOP, z_d, is inversely proportional to this disparity which can be written as

$$z_d = \frac{f_e p}{d_p} = f_e \frac{d_{shift}}{d_p} \tag{12}$$

where f_e is the effective focal length of the system, $d_{shift} = p + d_p$ is the total distance an elemental image is shifted, and d_p is the disparity. Therefore, a reconstructed image at z_d consists of all elemental images shifted by d_{shift} according to the shifting vector $\mathbf{s} = (s_x, s_y)$. The SM method implies reconstructed irradiance field (I_r) at $\mathbf{x} = (x, y)$ and $z = z_d$ parameterized by d_{shift} is a convolution of N shifted elemental images,

$$I_r(\mathbf{x}, d_{shift}) = \left(\prod_m I_s(\mathbf{x}) * \delta(\mathbf{x} + \mathbf{s} d_{shift}) \right)^{1/N}, \tag{13}$$

where $I_s(\mathbf{x})$ is an elemental image with a center given by the vector s. One may show (Sanchez-

Ortiga et al., 2020) that the reconstructed irradiance field at z_d simplifies to

$$I_r(\mathbf{x}, d_{shift}) = \left[\mathcal{O}(\mathbf{x}, d_{shift})^N + \Big[\prod_s \mathcal{O}\Big(\mathbf{x} + \mathbf{s} \times \big(d_{shift} - z\frac{d_p}{f}\big)\Big)\Big]_{z \neq f_e \frac{d_{shift}}{d_p}}\right]^{1/N} \tag{14}$$

where $\mathcal{O}(\cdot)$ is the 3D irradiance distribution of the object. The first term on the RHS of Equation 14 is the in-focus image at z_d to the N^{th} power. The second term are cross terms from the expansion in Eq. 13 that correspond to out-of-focus irradiance contained in the shifted images. For relatively sparse samples these terms represent a relatively weak contribution to the overall reconstruction. However, the photobleached dye gives a dark signal on a fluorescent background and these out-of-plane terms contribute more strongly.

Richardson-Lucy Deconvolution Algorithm

In order to reduce the contributions of out of plane fluorescence that appears in Eq. 14 of the SM method, one can characterize the point spread function (PSF) which describes the mapping of an emitter a distance z_k from the NOP to its projection onto the camera sensor at the NIP. The captured lightfield is then a convolution of the 3D object irradiance distribution at z_k with the corresponding PSF.

Therefore, the true irradiance distribution can be obtained by "deconvolution" of the measured signal by the modelled (Guo et al., 2019; Broxton et al., 2013; Stefanoiu et al., 2020a), or measured (Cong et al., 2017) PSF. While substantial effort has been dedicated to developing these methods for standard lightfield microscopy (plenoptic 1.0) (Broxton et al., 2013), recent developments for FIMic (Guo et al., 2019; Stefanoiu et al., 2019, 2020a,c; Cong et al., 2017) have proven promising. In particular the development of open-source tool by Stefanoiu et al. (2019, 2020a,c) have made these methods accessible, and we employ them here. While a full description of the deconvolution approach is outside of the scope of this work, we describe it summarily below and refer the reader to Stefanoiu et al. (2020a,c) for further details.

A wave-based forward light propagation model is used to describe the PSF as it propagates from the source, through the FIMic, and onto the camera sensor. To begin, a source point $o(0, 0, z = f_{MO} + z_k)$ a distance z_k from the NIP (see Fig. 3c), or $z = f_{MO} + z_k$, generates a wavefront $U_0(x, y; o)$ with an analytic expression derived from Rayleigh-Sommerfeld theory. This wavefront is propagated through a high numerical-aperture microscope objective according to the Debye scalar integral theory, to give a wavefront distribution at the back focal (Fourier) plane of the objective $U_{AS}(x_{as}, y_{as}; o)$ where (x_{as}, y_{as}) stands for the lateral coordinate at the aperture stop of the microscope objective. From the aperture, stop the $4 - f$ relay system does not necessitate modelling as the wavefront on the object side of the MLA is a magnified version of the wavefront at the aperture stop (U_{AS}) *i.e.*,

$$U_{MLA-}(x_{mla}, y_{mla}; o) = U_{AS}\Big(\frac{x_{mla}}{M_{relay}}, \frac{y_{mla}}{M_{relay}}; o\Big), \tag{15}$$

where $M_{relay} = f_2/f_1$ and a magnification of unity implies $U_{MLA-} = U_{AS}$. Light is propagated through the MLA using a 2D replication operator that accounts for the geometry of the MLA as

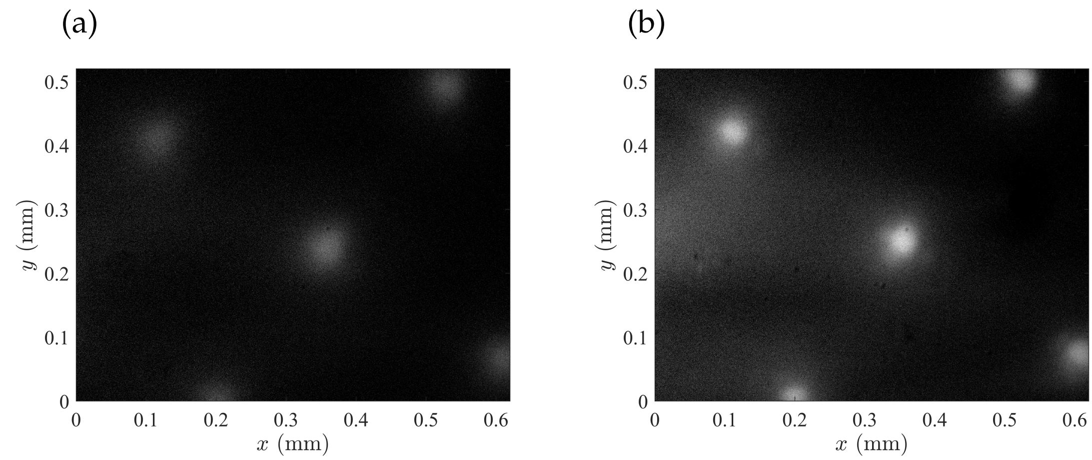

Figure 4. Confocal images in a plane parallel to the wall. (a) Wall normal distance of less than 50 µm. (b) Wall normal distance is close to the boundary layer thickness of $z = 2.8(\nu/\alpha)^{1/2} = 600$ µm (Eq. 4 and Table 1). The image in (a) at the wall is contrast enhanced by a factor of 2 with respect to (b).

the phase and amplitude are modified due to the change in optical path through each lens in the array. The result is the wavefront on the image side of the MLA U_{MLA+}. The final step is to employ the Rayleigh-Sommerfeld diffraction solution to propagate the lightfield to the sensor plane over a distance f_{MLA} which results in $U_{sens}(x_s, y_s; \mathrm{o})$.

The result of the forward light propagation model is $U_{sens}(x_s, y_s, \mathrm{o})$, which describes the wavefront incident on the sensor at (x_s, y_s) when the light is emitted from $\mathrm{o}(0, 0, z = f_{MO} + z_k)$. The goal of the deconvolution step is to start from a noisy sensor measurement $\mathbf{m} = (m_j)$ and recover the fluorescence photons emitted at a discrete voxel v_i, contained in a vector $\mathbf{v} = v_i$. Typically, Poisson statistics are assumed for $\mathbf{m}$, due to the low photon counts in fluorescence microscopy. We assume the same for the photobleached signal, where the absence of a photon due to the photobleaching process. Therefore a stochastic model is used: $\mathbf{m} \sim \mathrm{Poisson}(A\mathbf{v})$, where $A = (a_{ji})$ is the lightfield forward propagation model, which in essence is the FIMic PSF, given by $a_{ji} = |U_{sens}(x_{s,j}, y_{s,j}), \mathrm{o}_i|^2$. We note that o_i is the object space coordinate of the voxel i and $(x_{s,j}, y_{s,j})$ is the image space coordinate of the sensor pixel j. The Richardson-Lucy (Richardson, 1972; Lucy, 1974) iterative update scheme is used to perform the deconvoution with 10 iterations. The one step late (OSL) algorithm is implemented to preserve sharp features and readers are refered to Stefanoiu et al. (2020b) for further details. For 28 planes separated by R_{zF} (the same resolution as for the SM reconstruction) the computation takes 240 s. We note that the forward propagation model permits arbitrary axial resolution, although there is a practical limit to the resolution obtained.

4. Results

In this section we present the raw data for the photobleached MTV signal. In Section 4.1 the confocal microscope data is presented and in Section 4.2 the FIMic data is presented.

4.1. Confocal Microscopy

The confocal microscope (Fig. 3a) was fixed to a traverse and translated in the wall normal direction over roughly 1 mm to obtain images of the photobleached signal over the entire boundary layer. The expected resolution of the confocal microscope was given in Table 2. Figure 4 presents two images, one taken within the first 50 µm of the boundary layer (Fig. 4a) and one closer to the edge of the boundary layer, $z = \ell_\nu$. The background corrected image is $I_c = I_{bg} - I$ where I_{bg} is a background image without photobleaching, and I is the instantaneous photobleached image. The operation leaves the beamlets as white spots on a dark background, although the true signal is a dark signal on a fluorescent background. In general, the images closer to the wall have worse contrast and the beamlets appear slightly more diffuse. The confocal image at $z < 50$ µm has a peak in intensity (contrast) roughly half that of the image taken near the boundary layer.

4.2. FIMic : Shift and Multiply & Richardson-Lucy Deconvolution reconstruction

The raw data of the FIMic implementation is given in figure 3(d). The same background corrected operation is carried out and several photobleached beamlets are apparent. However, for both SM and Richardson-Lucy deconvolution, each respective method is performed both on a series of background images as well as photobleached images. Reconstruction in both cases occurs over a wall normal distance of roughly 1 mm in increments of $R_{zF} = 34$ µm.

The resulting reconstructed plane for SM and Richardson-Lucy Deconvolution (RLD) is given in Figure 5. The two reconstruction methods are compared in Figure 5(a-b) at $z = 30$ μm. Visually, the beamlets are much thinner in RLD than in SM. The cross-sectional cut through $x = 0.8$ mm in Figure 5(c) highlights this difference. The FWHM of the beamlets for the RLD, SM, and Confocal data are $[41,\ 70,\ 71]$µm. The data from RLD is close to the aberration free estimate of $w_0 \sim 28$ µm, although it is not clear what the source of anisotropy is in the RLD reconstruction of the beamlets, which degrades the obtained value. The offset in the SM data appears to be due to global shift in the background images with respect to the photobleached images.

The data reconstructed in a plane close to the edge of the boundary layer, $z = \ell_\nu$ are given in figure 5(d-e). Similar to the confocal measurements, the strength of the RLD signal is slightly noisier at $z = 30$ µm than at $z = \ell_\nu$. Interestingly, the beamlet thickness has increased slightly with the $FWHM = [60,\ 90,\ 60]$µm for the RLD, SM, and Confocal, respectively. It appears that the RLD data outperforms the SM in reconstructing beamlets that are close to what is expected theoretically in both near wall and edge of the boundary layer measurements.

A 3D rendering of the reconstructed beamlets using SM is given in Figure 6(a) and RLD in Figure 6(b). The "milky" appearance of the SM data is immediately apparent and likely due to the stronger presence of out-of-plane fluorescence. On the other hand the RLD data do not suffer from this effect to the same extent. The beamlets appear thinner for RLD than SM and in both cases the beamlets appear to have slightly thicker waists for distances farther from the wall.

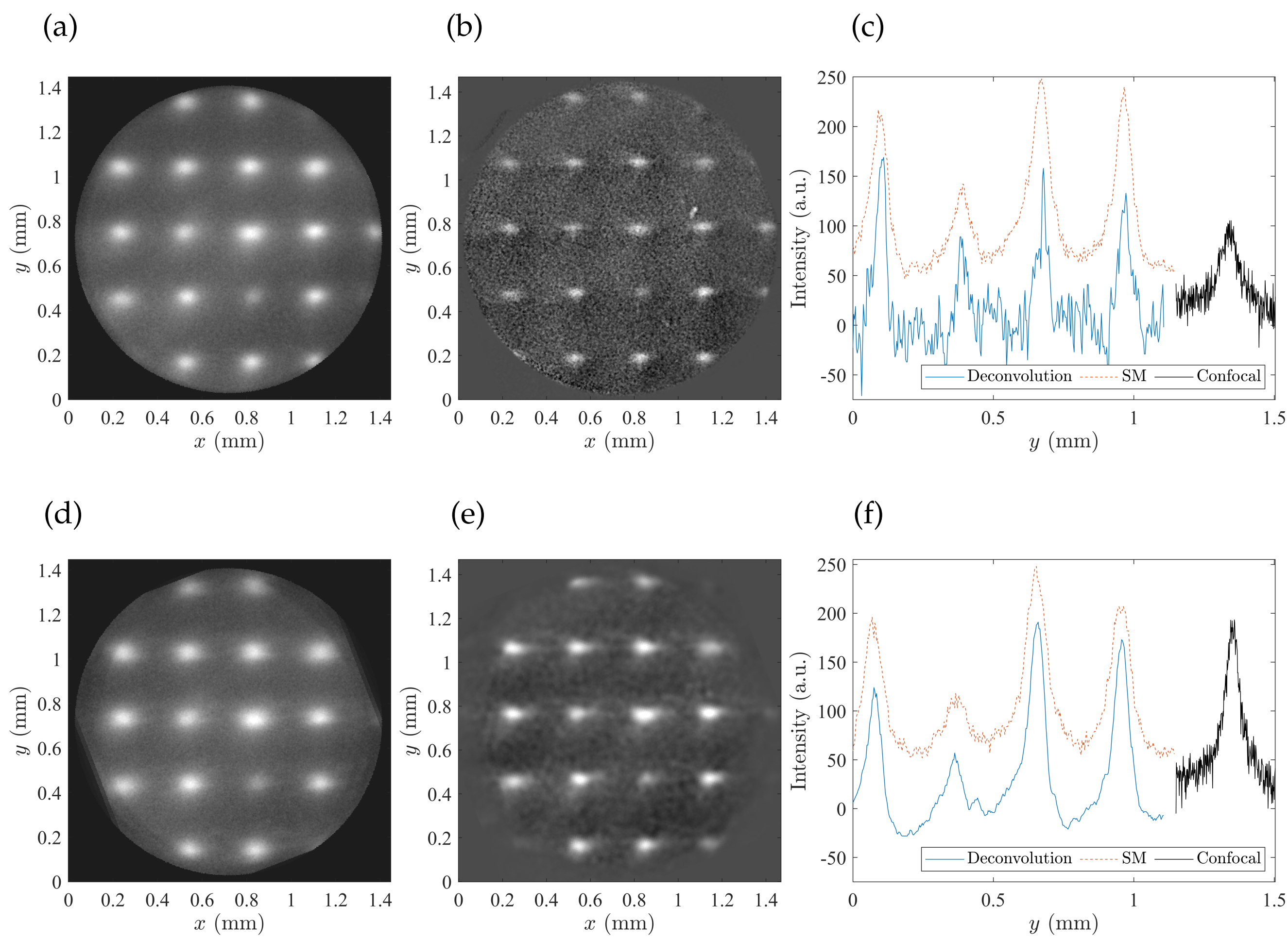

Figure 5. Comparison of Shift and Multiply, Deconvolution, and confocal microscopy images of a photobleached MTV signal (images are inverted for clarity). (a-c) Reconstructed at $z = 34$ µm in the wall normal direction. (a) SM reconstruction (b) Deconvolution reconstruction. (c) Comparison of cross-section in the y direction at $x = 0.85$ mm. (d-f) Reconstructed at the edge of the boundary layer (d) SM reconstruction (e) Deconvolution reconstruction. (f) Comparison of cross section in the y direction at $x = 0.85$ mm. ($z = 2.8(\nu/\alpha)^{1/2}$, Eq. 4)

4.3. Velocimetry Measurements

For both the Confocal Microscope and FIMic - RLD data velocimetry measurements are made by reconstructing individual planes and cross-correlating a undeformed beamlet with a beamlet advected by the flow 100 µs later. A post-processing code inspired by on the "sum-of-correlations" technique commonly used in PIV (Meinhart et al., 1999) is implemented to calculate the average particle displacement in the boundary layer. This technique gives similar results as measuring the displacement of the weighted center-of-mass for each beamlet. Due to long processing times of the RLD data, only 750 images were obtained, which did not permit adequate statistical convergence of the fourteen individual beamlets visible in figure 6(b). To increase the statistical weight of the ensemble, we combined all fourteen beamlets into a single ensemble, giving adequate statistics to obtain the results in Figure 7. We see that the data fall relatively well on the predictions of the Schlichting model for the velocity profile of an axisymmetric boundary layer in Equation 2. In

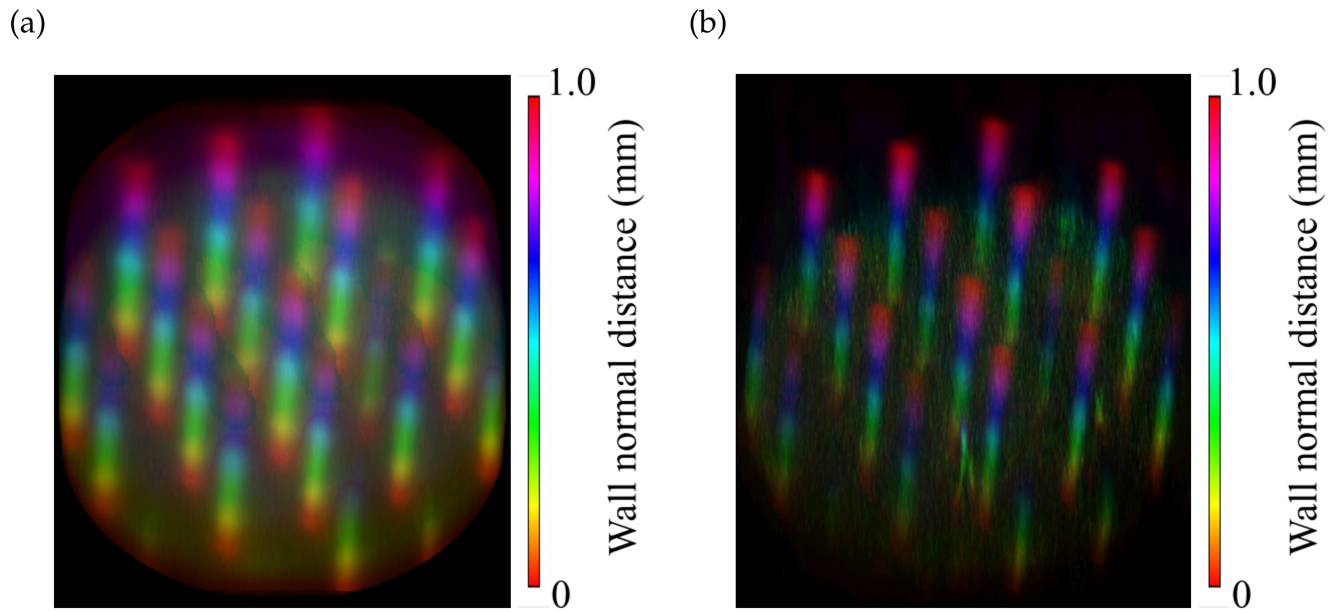

Figure 6. Comparison of 3D rendering with different reconstruction techniques for undeformed beamlets. (a) Shift and Multiply (b) Richardson-Lucy iterative Deconvolution (RLD).

particular we find that the prediction of the boundary layer thickness $\ell = 2.8(\nu/\alpha)^{1/2}$ in Equation 4 is a reasonable approximation to the data. The confocal microscope data also fit relatively well. Nevertheless, we do observe significant dispersion in the data which is more likely due to the stage of code development than statistical representation. We observe some spurious, non-physical events that are included in the statistical ensemble. There are certainly unresolved issues due to the nature of the "co-axial" measurement being made that may also contribute to these results which contribute to our inability to measure low ($U/U_0 < 0.2$) velocities.

5. Discussion

FIMic is a useful tool for microscopy where, similar to conventional orthographic microscopes, no parallax is observed in the images formed by each microlens. However, unlike conventional microscopes where magnification is constant independent of the depth of field, the 3D PSF of FIMic varies both in the lateral and axial directions. In particular reconstructions at different axial depths correspond to variations in the wavefront at the aperture stop of the microscope. This complex behavior in the imager is accounted for in the reconstruction techniques, both in SM and deconvolution based methods that rigorously simulate (or measure) the 3D PSF. The approach adopted using RLD does not fully take into account the wavefront passing through an optical window and fluid medium with an index of refraction different than air. Future modelling efforts will take this into account.

One challenge of the present technique, or any MTV technique near a wall, is that as a tube of tagged fluid that is stretched, its local diameter must also shrink. For small velocities close to

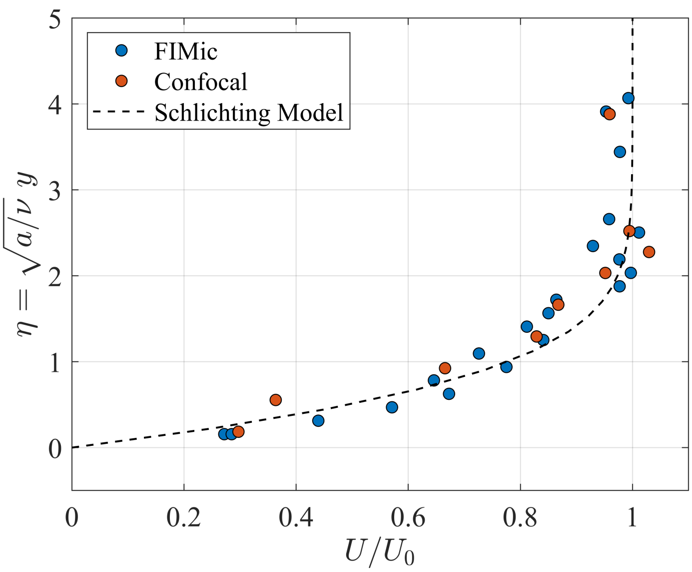

Figure 7. Velocimetry measurements comparing FIMic data using the Deconvolution approach with data obtained with a confocal microscope. The data fit the predictions of the Schlichting model relatively well.

the wall, but where the velocity gradient is strongest, a "thin" beam may only be displaced by a fraction of the "larger" cross-section at another wall normal distance. Therefore, reconstructing these may be difficult, especially in a co-axial configuration, despite the optical sectioning capacity of the instrument. We may need to make the beams thicker to minmize this effect.

We note that an arbitrarily thick write beam may provide too much out of plane fluorescence that overwhelms the photobleached signal. This is why we illuminate at an oblique (45°) angle with respect to the optical axis. The contributions of out of plane fluorescence further prevent us from aligning the read laser beam with the optical axis, which would simplify deployment. We are currently investigating new illumination strategies to mitigate these effects.

Further development of the RLD algorithm is necessary and the use of priors, in particular seeding the algorithm with a rapid SM reconstruction, may improve reconstruction ability as well as speed. Currently, 28 reconstructed planes separated by $34\ \mu m$ takes roughly 4 minutes per image to process. The resources developed by Stefanoiu et al. (2019, 2020a,c,b) also provide capability for super-resolution for sub-pixel resolution. However, the relatively diffuse nature of the photobleached signal may place a limit on the bandwidth gain that can be achieved by these algorithms.

6. Conclusions

We have adapted a Fourier Integral Microscope to MTV, which permits 3D-2C measurements in a fluid flow when using photobleached Rhodamine 6G as a flow tracer. To advance the instrument, we have designed and constructed an axi-symmetric stagnation jet with an adjustable boundary layer thickness and viscous length scale. Using state of the art computational imaging techniques we have shown that it is possible to reconstruct a 3D signal and make velocity measurements.

The Richardson-Lucy Deconvolution method outperforms the Shift and Multiply method and is capable of resolving close to the theoretical beamlet width. First ever measurements with this instrument are coherent with the theory of an axi-symmetric stagnation jet.

Further work is needed for implementing both velocimetry and reconstruction codes, in particular super-resolution algorithms. One challenge encountered during these measurements was the inability to measure velocities for the strongest gradients, which may limit the ultimate resolution of wall shear stress. We believe that this can be overcome by better processing and optimized illumination.

Acknowledgements

The authors acknowledge the support of the Nuclear Science and Security Consortium Fellowship and an ONR grant N00014-20-1-2672 managed by Dr. Peter Chang.

Nomenclature

MTV	Molecular Tagging Velocimetry
PIV	Particle Imaging Velocimetry
FIMic	Fourier Integral Microscopy
CM	Classic (Confocal) Microscopy
EI	Elemental Image
R6G	Rhodamin 6G
MLA	Micro Lens Array
TESI	Talbot Effect Structured Illumination
MO	Microscope Objective
NOP	Native Object Plane
NIP	Native Image Plane
SS	Shift and Sum Approach
SM	Shift and Multiply Approach
OSL	One Step Late Algorithm
RLD	Richardson-Lucy Deconvolution
z	optical axis
(x, y)	Lateral Coordinates
W_0	Bulk nozzle fluid velocity [m s^{-1}]
W	Axial fluid velocity [m s^{-1}]
U	Radial fluid velocity [m s^{-1}]
α	Stagnation Jet Parameter [s^{-1}]
L	Nozzle to wall distance [m]
ν	Kinematic viscosity [m^2 s^{-1}]

η	Self-similar variable [m^{-1}]
ℓ	boundary layer thickness [m]
ℓ_ν	viscous length scale [m]
Re_ν	Karman number [-]
NA	Numerical Aperture (Microscope Objective) [-]
NA_{ml}	Numerical Aperture (MLA) [-]
NA_{eff}	Effective Numerical Aperture of FIMic [-]
f_m (f_{mla})	Micro Lens focal length [m]
w_0	Diffraction Limited Beamlet Waist [m]
A_m	Optical Aberration Coefficient [-]
w_i	Micro lens aperture [m]
p_0	MLA pitch [m]
λ	Wave length [m]
z_T	Talbot Distance [m]
w_L	Initial (UV) laser beam diameter [m]
n_0	number of micro lenses illuminated [-]
$p(z)$	Talbot carpet periodicity at z [-]
$Q,\ R$	Co-prime integers for Talbot periodicity [-]
K	Third integer for Talbot periodicity [-]
f_{MO}	Microscope Objective focal length [m]
f_1	Tube Lens focal Length (First 4-f lens) [m]
f_2	Focal length (second 4-f lens) [m]
Δ_{z0}	Depth of Field (CM) [m]
Δ_{zF}	Depth of Field (FIMic) [m]
Δ_{wave}	Wave optics contribution DoF [m]
Δ_{geo}	Geometric optics contributino DoF [m]
n	Index of refraction [-]
p_{pix}	Pixel pitch [m]
R_{xy0}	Lateral Resolution (CM) [m]
R_{z0}	Axial Resolution (CM) [m]
R_{xyF}	Lateral Resolution (FIMic) [m]
R_{zF}	Axial Resolution (FIMic) [m]
D_{as}	Aperture stop diameter [m]
p	pitch of MLA [m]
N	Number of sub-apertures
γ	Pixel Shift [-]
z_d	Axial Distance (NOP-NIP) [m]
f_e	Effective focal length (reconstruction) [m]
d_p	Disparity [m]
d_{shift}	EI shift distance [m]

$\mathrm{s} = (s_x, s_y)$	Shifting vector [-]
I_r	Irradiance Field (object space) [-]
I_s	Irradiance Field (image space) [-]
δ	Dirac operator [-]
$\mathcal{O}(\cdot)$	True Irradiance Field (object space) [-]
$\mathrm{o}(0, 0, z)$	Source Illumination [-]
$U_0(x, y; \mathrm{o})$	Source Wavefront [-]
(x_{as}, y_{as})	Lateral position at aperture stop [m]
$U_{AS}(x_{as}, y_{as})$	Wave front at aperture stop [-]
M_{relay}	Relay magnification [-]
(x_{mla}, y_{mla})	Lateral position aperture at MLA [m]
$U_{MLA-}(x_{mla}, y_{mla})$	Wave front at object side of MLA [-]
$U_{MLA+}(x_{mla}, y_{mla})$	Wave front at image side of MLA [-]
(x_s, y_s)	Lateral position on sensor [m]
$U_{sens}(x_s, y_s)$	Wavefront at sensor [-]
$\mathrm{m} = m_j$	Realization of measurement m_j at sensor [-]
$\mathrm{v} = v_i$	Realization of source irradiance in voxel i [-]
$A = (a_{ji})$	Light field Forward propagation model [-]

References

Atkinson, C., & Soria, J. (2009). An efficient simultaneous reconstruction technique for tomographic particle image velocimetry. *Exp. Fluids*, *47*(4-5), 553–568.

Barlow, J. B., Rawe, W. H., & Pope, A. (1999). *Low-speed wind tunnel testing*. John Wiley & Sons.

Broxton, M., Grosenick, L., Yang, S., Cohen, N., Andalman, A., Deisseroth, K., & Levoy, M. (2013). Wave optics theory and 3-D deconvolution for the light field microscope. *Opt. Express*, *21*(21), 25418.

Cong, L., Wang, Z., Chai, Y., Hang, W., Shang, C., Yang, W., … Wen, Q. (2017). Rapid whole brain imaging of neural activity in freely behaving larval zebrafish (Danio rerio). *Elife*, *6*, 1–20.

Fort, C., André, M. A., Pazhand, H., & Bardet, P. M. (2020). Talbot-effect structured illumination: pattern generation and application to long-distance μ -MTV. *Exp. Fluids*, *61*(2), 1–21.

Fort, C., & Bardet, P. M. (2021). Efficient photobleaching of rhodamine 6G by a single UV pulse. *Appl. Opt.*, *60*(22), 6342.

Gibson, A. H. (1910). On the Flow of Water through Pipes and Passages having Converging or Diverging Boundaries. *Proc. R. Soc. London. A. Math. Phys. Sci.*, *83*(563), 366–378.

Guo, C., Wenhao, L., Hua, X., Li, H., & Jia, S. (2019). Fourier light-field microscopy. *Opt. Express*, *27*(27), 25573–25594.

H. Kreplin. (1994). *Three-dimensional boundary layer and flow field data of an inclined prolate spheroid* (Tech. Rep. No. 303). AGARD advisory report.

Hong, S.-H., Jang, J.-S., & Javidi, B. (2003). Three-dimensional volumetric object reconstruction using computational integral imaging. *Opt. Express.*, *12*(3).

Huang, T., Liu, H.-L., Graves, N., Blanton, J., & Gowing, S. (2012). Measurements of flows over an axisymmetric body with various appendages in a wind tunnel: the darpa suboff experimental program. In *19th symposium on naval hydrodynamics.*

Kim, H., Groe, S., Elsinga, G. E., & Westerweel, J. (2011). Full 3D-3C velocity measurement inside a liquid immersion droplet. *Exp. Fluids*, *51*(2), 395–405.

Kim, H., Westerweel, J., & Elsinga, G. E. (2013). Comparison of Tomo-PIV and 3D-PTV for microfluidic flows. *Meas. Sci. Technol.*, *24*(2).

Levoy, M., Ng, R., Adams, A., Footer, M., & Horowitz, M. (2006). Light field microscopy. *ACM Trans. Graph.*, *25*(3).

Lucy, L. B. (1974). An iterative technique for the rectification of observed distributions. *Astron. J.*, *79*(6), 745.

Mehta, R. D., & Bradshaw, P. (1979). Technical notes of design for small low speed wind tunnels. *Aeronaut. J. R. Aeronaut. Soc.*(7), 1, 445, 446 448.

Meinhart, C. D., Wereley, S. T., & Santiago, J. G. (1999). PIV measurements of a microchannel flow. *Exp. Fluids*, *27*(5), 414–419.

Pope, S. B. (2010). *Turbulent flows*. Cambridge University Press.

Richardson, W. H. (1972). Bayesian-Based Iterative Method of Image Restoration. *J. Opt. Soc. Am.*, *62*(1), 1–8.

Sanchez-Ortiga, E., Scrofani, G., Saavedra, G., & Martinez-Corral, M. (2020). Optical Sectioning Microscopy through Single-Shot Lightfield Protocol. *IEEE Access*, *8*, 14944–14952.

Schlichting, H. (2017). *Boundary-layer theory*. Springer.

Schultz, M. (2007). Effects of coating roughness and biofouling on ship resistance and poweringy. *Biofouling.*, *23*(5).

Scrofani, G., Sola-Pikabea, J., Llavador, A., Sanchez-Ortiga, E., Barreiro, J. C., Saavedra, G., … Martínez-Corral, M. (2018). FIMic: design for ultimate 3D-integral microscopy of in-vivo biological samples. *Biomed. Opt. Express*, *9*(1), 335.

Stefanoiu, A., Page, J., Symvoulidis, P., Westmeyer, G. G., & Lasser, T. (2019). Artifact-free deconvolution in light field microscopy. *Opt. Express*, *27*(22), 31644.

Stefanoiu, A., Scrofani, G., Saavedra, G., Martínez-Corral, M., & Lasser, T. (2020a). Deconvolution in Fourier integral microscopy. (May), 18.

Stefanoiu, A., Scrofani, G., Saavedra, G., Martínez-Corral, M., & Lasser, T. (2020b). *Deconvolution in Fourier integral microscopy.* Proc. SPIE 11396, Computational Imaging V, 1139601.

Stefanoiu, A., Scrofani, G., Saavedra, G., Martínez-Corral, M., & Lasser, T. (2020c). What about computational super-resolution in fluorescence Fourier light field microscopy? *Opt. Express*, *28*(11), 16554.

Talamelli, A., Persiani, F., Fransson, J. H., Alfredsson, P. H., Johansson, A. V., M Nagib, H., ... Monkewitz, P. A. (2009). CICLoPE - A response to the need for high Reynolds number experiments. *Fluid Dyn. Res.*, *41*(2), 1–21.

van Doorne, C. W. H., & Westerweel, J. (2007). Measurment of laminar, transitional and turbulent pipe flow using stereoscopic-piv. *Exp. Fluids*, *42*.

Winkel, E. S., Cutbirth, J. M., Ceccio, S. L., Perlin, M., & Dowling, D. R. (2012). Turbulence profiles from a smooth flat-plate turbulent boundary layer at high reynolds number. *Exp. Therm. Fluid Sci.*, *40*.

Worth, N. A., & Nickels, T. B. (2008). Acceleration of Tomo-PIV by estimating the initial volume intensity distribution. *Exp. Fluids*, *45*(5), 847–856.